



**HAL**  
open science

# Phosphine Oxide Porous Organic Polymers Incorporating Cobalt(II) Ions: Synthesis, Characterization, and Investigation of H-2 Production

Giulia Bonfant, Davide Balestri, Jacopo Perego, Angiolina Comotti, Silvia Bracco, Matthieu Koepf, Marcello Gennari, Luciano Marchio

► **To cite this version:**

Giulia Bonfant, Davide Balestri, Jacopo Perego, Angiolina Comotti, Silvia Bracco, et al.. Phosphine Oxide Porous Organic Polymers Incorporating Cobalt(II) Ions: Synthesis, Characterization, and Investigation of H-2 Production. ACS Omega, 2022, 7 (7), pp.6104-6112. 10.1021/acsomega.1c06522 . hal-03632966

**HAL Id: hal-03632966**

**<https://hal.science/hal-03632966>**

Submitted on 25 Aug 2022

**HAL** is a multi-disciplinary open access archive for the deposit and dissemination of scientific research documents, whether they are published or not. The documents may come from teaching and research institutions in France or abroad, or from public or private research centers.

L'archive ouverte pluridisciplinaire **HAL**, est destinée au dépôt et à la diffusion de documents scientifiques de niveau recherche, publiés ou non, émanant des établissements d'enseignement et de recherche français ou étrangers, des laboratoires publics ou privés.

# Phosphine Oxide Porous Organic Polymers Incorporating Cobalt(II) Ions: Synthesis, Characterization, and Investigation of H<sub>2</sub> Production

Giulia Bonfant, Davide Balestri, Jacopo Perego, Angiolina Comotti, Silvia Bracco, Matthieu Koepf, Marcello Gennari, and Luciano Marchiò\*



Cite This: *ACS Omega* 2022, 7, 6104–6112



Read Online

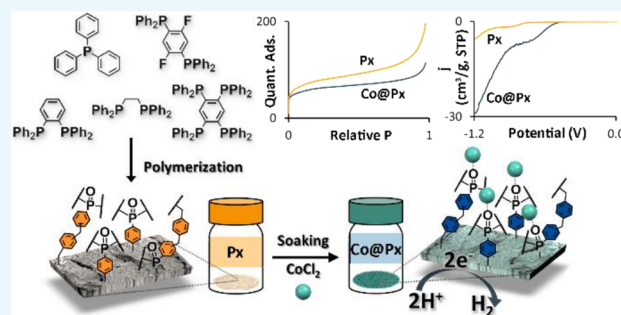
ACCESS |

Metrics & More

Article Recommendations

Supporting Information

**ABSTRACT:** Suitably functionalized porous matrices represent versatile platforms to support well-dispersed catalytic centers. In the present study, porous organic polymers (POPs) containing phosphine oxide groups were fabricated to bind transition metals and to be investigated for potential electrocatalytic applications. Cross-linking of mono- and di-phosphine monomers with multiple phenyl substituents was subject to the Friedel–Crafts (F–C) reaction and the oxidation process, which generated phosphine oxide porous polymers with pore capacity up to 0.92 cm<sup>3</sup>/g and a surface area of about 990 m<sup>2</sup>/g. The formation of the R<sub>3</sub>P·BH<sub>3</sub> borohydride adduct during synthesis allows to extend the library of phosphine-based monomeric entities when using FeCl<sub>3</sub>. The porous polymers were loaded with 0.8–4.2 w/w % of cobalt(II) and behaved as hydrogen evolution reaction (HER) catalysts with a Faradaic efficiency of up to 95% (5.81 × 10<sup>-5</sup> mol H<sub>2</sub> per 11.76 C) and a stable current density during repeated controlled potential experiments (CPE), even though with high overpotentials (0.53–0.68 V to reach a current density of 1 mA·cm<sup>-2</sup>). These studies open the way to the effectiveness of tailored phosphine oxide POPs produced through an inexpensive and ecofriendly iron-based catalyst and for the insertion of transition metals in a porous architecture, enabling electrochemically driven activation of small molecules.



## INTRODUCTION

Many classes of porous materials were devised in the past decades, with a great variety of chemical composition, structural order, and functions. These materials encompass purely inorganic zeolites,<sup>1</sup> hybrid metal organic-frameworks (MOFs, crystalline),<sup>2–5</sup> and purely organic materials<sup>6</sup> like covalent organic frameworks (COFs, crystalline).<sup>7,8</sup> The functional properties of these materials are strongly determined by the permanent porosity, large accessible surface, and size and shape of the pores.<sup>3,9–11</sup> More recently, amorphous porous organic polymers (POPs) have been developed, showing a higher stability than MOFs and COFs, and they can be prepared with a number of chemical functionalities within the cavities. Symmetric aromatic synthons, with tetrahedral- or trigonal-planar geometries, condensed through controlled and directional synthetic methodologies, produced porous materials with uniform pore size distribution and high capacity.<sup>12–17</sup> POPs can also be prepared with more conformationally flexible monomers with nonunivocal position of the linkage bond between monomers and linkers.<sup>18,19</sup> Similar to other porous materials, POPs can be prepared by incorporating into the framework Lewis basic sites that can serve as electron-donor systems for metal centers, and thus are suitable for proton transport,<sup>20</sup> or the capture of volatile species.<sup>21</sup>

Additionally, POPs have been investigated in the domain of heterogeneous catalysis,<sup>18,22–25</sup> usually after the incorporation of metal centers.<sup>26–28</sup> In particular, porous frameworks containing phosphine groups coordinated to metal ions were successfully applied in catalysis.<sup>29–32</sup> Although phosphine oxide functional groups can bind metal ions<sup>33</sup> and promote the interaction with heavy elements, providing anchoring sites for metals in the active sites of catalysts, to date, rarely they are incorporated in POPs.<sup>34,35</sup> A high degree of chemical tunability makes POPs potentially adapted to applications in the energy conversion domain, including electrocatalysis for small molecule activation.<sup>36</sup> However, while the electrocatalytic applications of MOFs<sup>37–41</sup> and COFs<sup>42–44</sup> are extensively explored, the study of POP-based electrocatalysts is only in its infancy.<sup>45–48</sup>

In this work, a series of porous organic polymers bearing P=O functional groups was synthesized and loaded with metal ions to obtain hybrid materials containing highly

**Received:** November 19, 2021

**Accepted:** January 5, 2022

**Published:** February 11, 2022



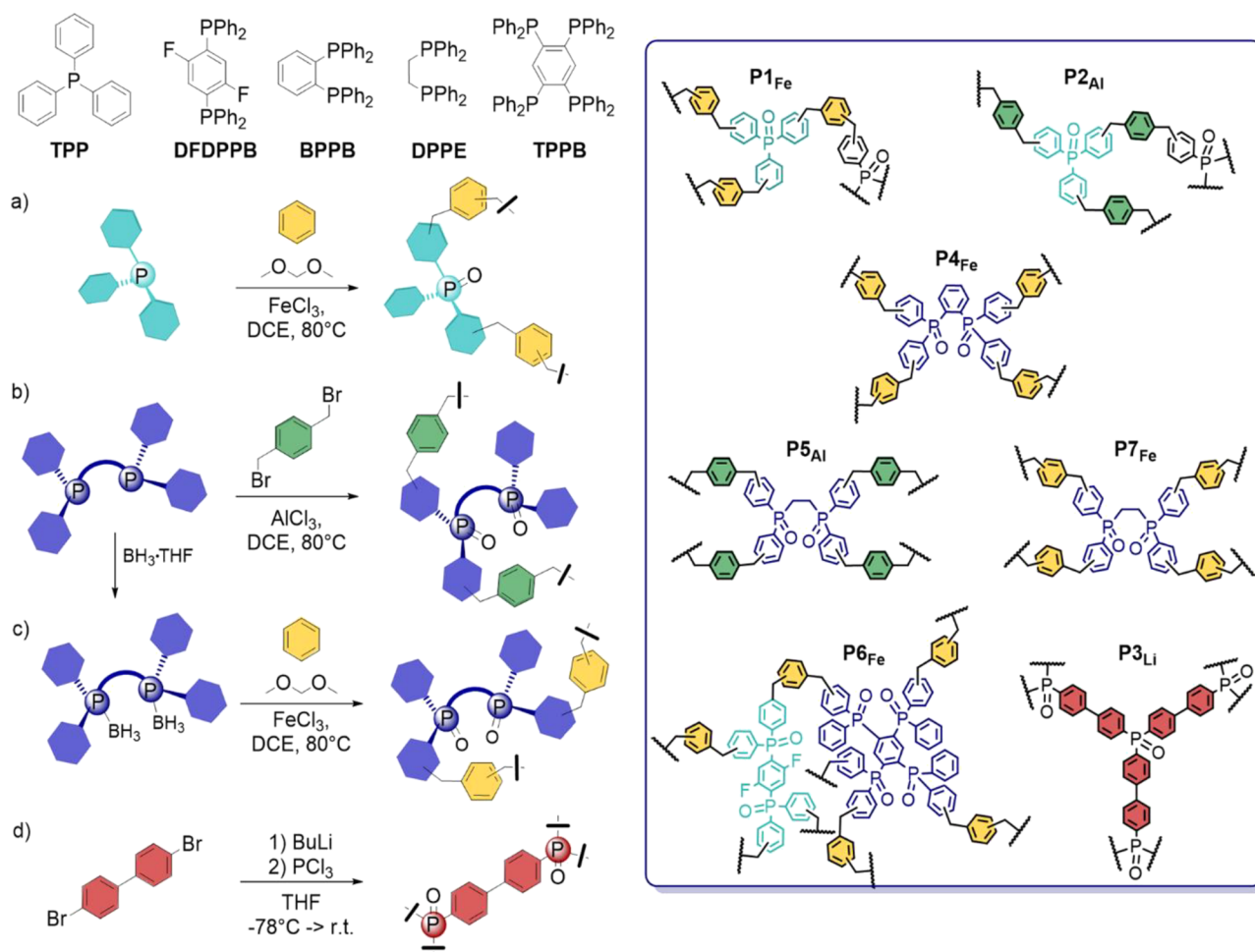


**Figure 1.** Synthetic pathways (left, a–d) and polymers described in this work (right).

dispersed, yet accessible, catalytic sites, which promoted electrocatalysis for hydrogen evolution.

Specifically, the porous frameworks have in common the  $R_3P=O$  structural motif covalently bound within the robust architecture. Various synthetic procedures were applied to prepare phosphine oxide POPs, namely, the Friedel–Crafts (F-C) reaction with  $FeCl_3$  or  $AlCl_3$  on phenylphosphines or a two-step procedure starting from trichlorophosphine.<sup>30</sup> The P atoms of the resulting porous polymers were oxidized, providing the  $P=O$  moiety that was demonstrated to be a good anchoring site for transition metals.<sup>49</sup>

These processes yielded porous frameworks containing isolated phosphine oxide building units ( $P1_{Fe}$ ,  $P2_{Al}$ , and  $P3_{Li}$ , Figure 1) and bidentate units in which two adjacent phosphine oxide units can cooperate to increase the metal-binding ability ( $P4_{Fe}$ ,  $P6_{Fe}$ ,  $P7_{Fe}$ , and  $P5_{Al}$ ).  $N_2$  gas-adsorption measurements of the polymers show permanent porosity in both the micro- and mesopore regions, facilitating the diffusion of metal species for the formation of catalytic metal centers. The materials were characterized using thermal methods, multinuclear solid-state nuclear magnetic resonance (NMR) and energy-dispersive X-ray spectroscopy (EDX). In a proof-of-concept study, we screened the hydrogen evolution reaction (HER) activity of the Co-containing materials under neutral pH conditions, which are more environmentally benign with respect to HER in acidic and basic electrolytes,<sup>50–54</sup> even if more challenging to achieve efficient catalysis.<sup>54</sup>

## RESULTS AND DISCUSSION

**Synthesis.** Porous organic polymers were obtained by the F-C reaction;<sup>12</sup> in particular, phosphine monomers and external linkers such as benzene with formaldehyde dimethyl acetal (FDA) or 1,3-bis(bromomethyl)benzene were mixed together with a Lewis acid ( $FeCl_3$  or  $AlCl_3$ ) to promote polymerization, Figure 1. In the synthesis, we used monodentate or bidentate P-donors; specifically, the bidentate and conformationally rigid monomers [BPPB (1,2-bis-(diphenylphosphino)benzene), and TPPB (1,2,4,5-tetrakis-(diphenylphosphanyl)benzene)] gave rise to P-POPs with the two donor functions properly oriented to provide chelation to the metal center. In the case of bidentate DPPE (1,2-bis-(diphenylphosphanyl)ethane), the complexation of P with  $BH_3$  was necessary to prevent the scavenging effect of phosphine groups. The synthesis of compound  $P3_{Li}$  involved the polymerization of the 4,4'-dibromobiphenyl precursor treated with butyllithium and  $PCl_3$ .

**Characterization of the Frameworks.** The materials prepared were characterized by thermal analysis, showing thermal stability above 400 °C (Figures 2 and S21–S27). The thermogravimetric analysis (TGA) profile of  $P3_{Li}$  was different from that of the other systems, and it showed a sharp multistage decomposition profile with the first weight loss (49%) between 300 and 455 °C and the second weight loss (40%) from 530 to 640 °C. The Fourier transform infrared (FT-IR) spectra of  $P1$ – $P7$  showed similarities with the

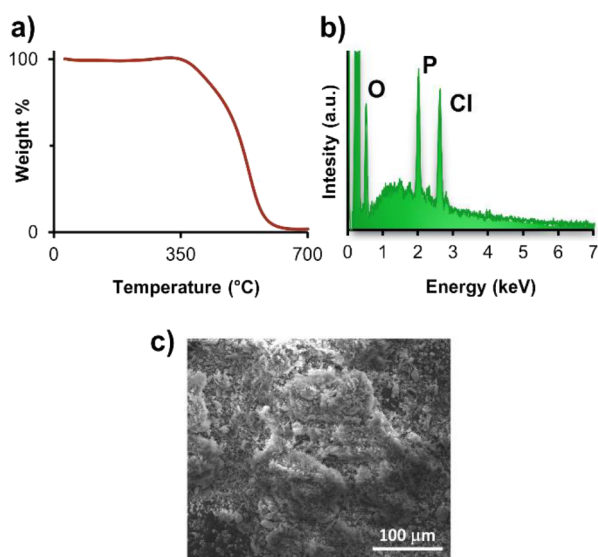


**Figure 2.** Characterization of  $P4_{Fe}$ . (a) TGA in the 25–700 °C temperature range under oxygen flux. (b) EDX spectrum. Chlorine signal from the residual DCE solvent. (c) SEM image.

corresponding phosphine precursors, even though the IR bands were usually larger in the frameworks. All the systems, except  $P3_{Li}$ , exhibited 2900–3000  $cm^{-1}$  C–H stretching bands, which were associated to the methylene bridge linking the aromatic moieties, Figures S14–S20.

One-dimensional (1D)  $^{13}C$ ,  $^1H$ , and  $^{31}P$  and two-dimensional (2D)  $^1H$ – $^{13}C$  NMR spectroscopy were used to study

the structural organization at the molecular level.  $^{13}C$  spectra of the porous polymers showed peaks between 110 and 150 ppm easily ascribed to the aromatic rings of monomeric units, Figure 3. Additional signals were present in the aliphatic region for F-C reaction polymers, irrespective of the monomer. The complex pattern was due to multiple alkylation of the aromatic rings.

$^{13}C$  Cross-Polarization Magic-Angle-Spinning (CP MAS) NMR spectra of the compounds  $P1_{Fe}$ ,  $P4_{Fe}$ ,  $P6_{Fe}$ , and  $P7_{Fe}$  synthesized by the Fe-based F-C reaction exhibited a prominent signal at about  $\delta = 37$  ppm owing to the methylene bridges connecting the aromatic rings of monomer units. Moreover, minor alkyl and alkoxy ( $CH_3$ ,  $CH_2-O$  and  $CH_3-O$  at  $\delta = 16.8$ – $18.7$ ,  $56.5$ , and  $73.0$  ppm) originated by pendant groups were identified as already observed in porous aromatic polymers by the F-C reaction.<sup>55</sup> A lower content of chlorine-containing pendant groups resonated at 40–44 ppm together with ph- $CH_2$ -ph in the broad signal centered at 37 ppm. In  $^{13}C$  CP MAS spectra, the pendant group signals were intensified because of hydrogen-to-carbon magnetization transfer, while in the quantitative  $^{13}C$  MAS NMR spectra, they appeared to be negligible. In the case of Al-based F-C compounds ( $P2_{Al}$  and  $P5_{Al}$ ), we observed  $CH_2$ -bridging groups and  $CH_3$  pendants in the benzyl position (Figure S10). In  $P3_{Li}$ , the aromatic signals substantially dominated, encompassing the carbon–carbon signal of the diphenyl connecting group.<sup>30</sup>

The connectivity of methylene groups, which linked the aromatic rings in the F-C reaction was inferred by 2D  $^1H$ – $^{13}C$  NMR spectra, which provided evidence of the close spatial

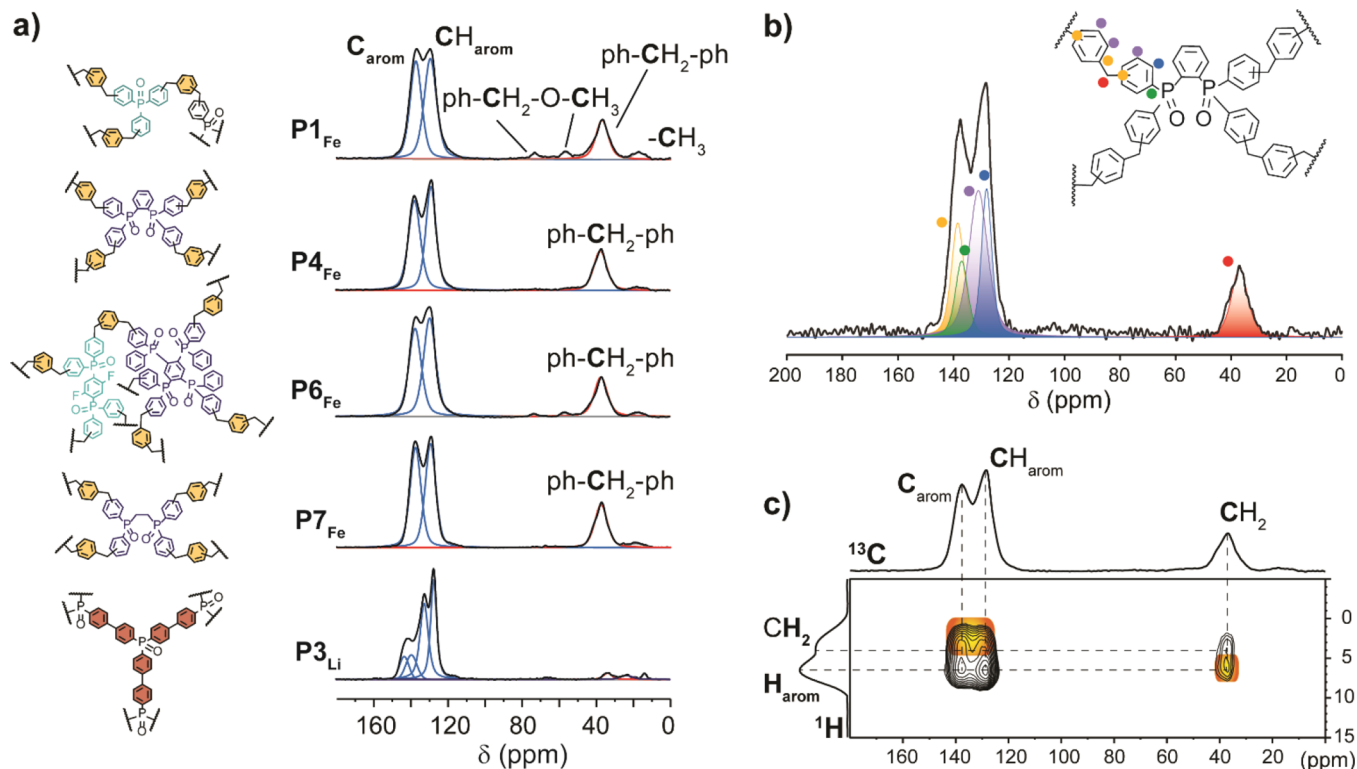


**Figure 3.** (a)  $^{13}C\{^1H\}$  CP MAS spectra of  $P1_{Fe}$ ,  $P4_{Fe}$ ,  $P6_{Fe}$ ,  $P7_{Fe}$ , and  $P3_{Li}$  materials performed at a spinning speed of 12.5 kHz and a contact time of 2 ms. (b) Quantitative  $^{13}C\{^1H\}$  MAS spectrum of  $P4_{Fe}$  performed at a spinning speed of 12.5 kHz and a recycle delay of 60 s. (c) 2D  $^1H$ – $^{13}C$  PMLG HETCOR NMR spectrum of  $P4_{Fe}$  performed at 12.5 kHz and a contact time of 2 ms. The cross-peaks, highlighted in orange, show the through-space interactions between the aromatic ring and the methylene moiety.

proximity between  $^1\text{H}$  and  $^{13}\text{C}$  nuclei. The 2D  $^1\text{H}$ - $^{13}\text{C}$  MAS spectrum of  $\text{P4}_{\text{Fe}}$  highlighted the aromatic hydrogens of the main architecture ( $\delta_{\text{H}} = 6.5$  ppm) correlated to the carbons of the bridging methylene groups ( $\delta_{\text{C}} = 37.3$  ppm), Figure 3. Likewise, the bridging  $\text{CH}_2$  hydrogens at  $\delta_{\text{H}} = 4.0$  ppm correlated with the aromatic carbons, confirming the reticulation of the monomers by the  $\text{CH}_2$  linkers. Moreover, the abundance of the  $\text{CH}_2$  linkers created using the synthetic procedure could be inferred by a quantitative analysis of the  $^{13}\text{C}$  MAS spectrum obtained with a long recycle delay of 60 s. The quantitative results of 1 methylene per 9 aromatic carbons were in agreement with the fact that all phenyls of the precursor are reacted and connected through  $-\text{CH}_2-$  benzene- $\text{CH}_2-$  bridges (Table S2).

According to the  $^{31}\text{P}$  SS NMR spectra, the signals of the phosphorus atoms resonated at about 30 ppm, in agreement with the presence of the  $\text{P}=\text{O}$  moiety. In  $\text{P3}_{\text{Li}}$ ,  $\text{P7}_{\text{Fe}}$ , and  $\text{P6}_{\text{Fe}}$  the minor peaks at  $\delta = -7.2$ ,  $-10.5$ , and  $-14.8$  ppm, respectively, suggested the minor presence of reduced aryl phosphorus (Figure S11). This result was in line with previous findings.<sup>30</sup> The  $^{19}\text{F}$  SS NMR spectrum of  $\text{P6}_{\text{Fe}}$  showed the peaks associated to the presence of aromatic fluorine atoms, Figure S13.

The porosity of the frameworks was assessed by  $\text{N}_2$  adsorption isotherms at 77 K, which exhibited a steep slope in gas uptake at very low relative pressures and a continuous increase at higher pressures, reflecting the simultaneous presence of micro- and meso-pores (Figure 4). We could

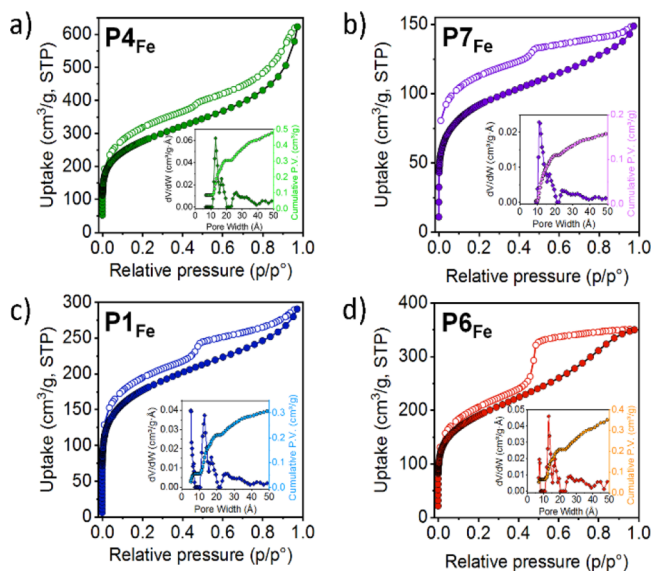


**Figure 4.**  $\text{N}_2$  physisorption isotherms at 77 K (adsorption, ●; desorption, ○) for  $\text{P4}_{\text{Fe}}$  (a),  $\text{P7}_{\text{Fe}}$  (b),  $\text{P1}_{\text{Fe}}$  (c), and  $\text{P6}_{\text{Fe}}$  (d). Adsorption and desorption branches are denoted by filled and empty symbols, respectively. Insets: differential and cumulative pore size distributions between 0 and 50 Å (dark and light colors, respectively).

observe that the highest surface area [Langmuir and Brunauer–Emmett–Teller (BET) surface areas of 1125 and 990  $\text{m}^2/\text{g}$ , respectively for  $\text{P4}_{\text{Fe}}$ ] was achieved by the rigid monomer structure in which four aromatic rings connected to two phosphorus atoms in the core protrude at different angles, ensuring the expansion of the framework in all directions. An analogous monomer, which contained a flexible ethyl group connecting the two phosphorus atoms, instead of a rigid

aromatic ring, allowed higher degrees of conformational freedom and did not generate a framework with a high surface area ( $\text{P7}_{\text{Fe}}$ ). Relatively high surface areas of 727 and 640  $\text{m}^2/\text{g}$  were obtained from the monomer triphenylphosphine bearing three phenyl rings. Interestingly, a number of aromatic rings greater than four did not produce any increase in both the surface area and the pore capacity, most likely as a result of the overcrowded reticulation on the same monomer ( $\text{P6}_{\text{Fe}}$ ). Hysteresis loops were observed between the adsorption and desorption branches. Such a behavior was indicative of the swelling of the network during sorption owing to capillary condensation in the mesopores, which caused some expansion in the network, as systematically observed in soft polymeric materials.<sup>16,56,57</sup> In the case of  $\text{P6}_{\text{Fe}}$ , the closure at  $P/P_0$  of about 0.4 in the hysteresis loop suggested the mesopore shrink to a less extent. Lower surface areas were obtained by the Al-based F-C frameworks (ESI).

**Complexation with Transition-Metal Ions.** The presence of binding sites within the frameworks was expected to promote the anchoring of transition-metal ions within the cavities. According to  $^{31}\text{P}$  NMR, the donor function was represented by  $\text{P}=\text{O}$ , which is suitable for hard transition-metal ions such as lanthanides or the first-row transition metals.<sup>49,58–60</sup> Hence, the frameworks were readily loaded with  $\text{Co(II)}$  by soaking the frameworks with tetrahydrofuran (THF) solutions of  $\text{CoCl}_2 \cdot 6\text{H}_2\text{O}$ . The products were extensively washed with THF to remove the excess metal not bound to the frameworks, until a colorless supernatant appeared. The loading of the materials could be easily appreciated by color change from white to green for  $\text{Co@P3}_{\text{Li}}$  (Figure 5), whereas  $\text{Co@P1}_{\text{Fe}}$ ,  $\text{Co@P4}_{\text{Fe}}$ , and  $\text{Co@P6}_{\text{Fe}}$

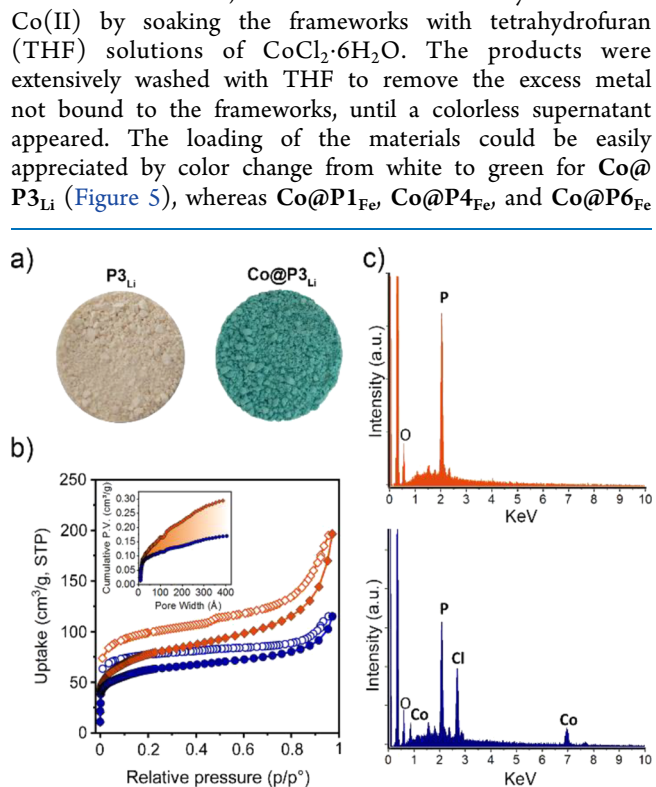


**Figure 5.** (a)  $\text{P3}_{\text{Li}}$  (white) and  $\text{Co@P3}_{\text{Li}}$  (green). (b)  $\text{N}_2$  adsorption isotherm at 77 K of  $\text{P3}_{\text{Li}}$  (orange) and  $\text{Co@P3}_{\text{Li}}$  (blue). Inset: cumulative pore size distributions. (c) EDX of  $\text{P3}_{\text{Li}}$  (orange) and  $\text{Co@P3}_{\text{Li}}$  (blue).

were brown powders (Figure S34). Energy-dispersive X-ray spectroscopy (EDX) confirmed the presence of the metal centers in the functionalized polymers, Figure 5. According to inductively coupled plasma-atomic emission spectroscopy (ICP-AES), the amount of cobalt anchored to the polymers was in the 0.8–4.2% w/w range, (Tables S5 and S6). The  $\text{N}_2$  adsorption isotherm of  $\text{P3}_{\text{Li}}$  at 77 K exhibited both micro- and

mesoporosity with notable swellability, as shown by the hysteresis loop, which closed to zero at a low partial pressure (Figure 5). In  $\text{P3}_{\text{Li}}$ , the mesopore fraction allowed easy access to the isolated  $\text{P}=\text{O}$  moieties from the diffusing species, thus favoring specific interactions with metal ions. Consistently,  $\text{Co@P3}_{\text{Li}}$  had a considerably reduced mesopore component, a lower surface area, and a shift of the pore width profile to lower values (Figure S30). On the other hand, the presence of the metal ions did not lead to an occlusion of the inner cavities, hence allowing the movement of small molecules toward and from the metal centers.

**HER Studies.** The electrocatalytic activity of the Co-loaded materials for the HER was explored by linear sweep voltammetry (LSV) in aqueous solution at neutral pH (phosphate buffer). In the case of  $\text{P1}_{\text{Fe}}$ ,  $\text{P4}_{\text{Fe}}$ ,  $\text{P6}_{\text{Fe}}$ , and  $\text{P3}_{\text{Li}}$ -modified electrodes, a significant increase in current density was observed in the range from  $\sim -0.4$  to  $-0.9$  V vs RHE range for metallated materials vs metal-free compounds (Figures 6 and S39, half-wave potentials =  $-0.75$  V for  $\text{P1}_{\text{Fe}}$

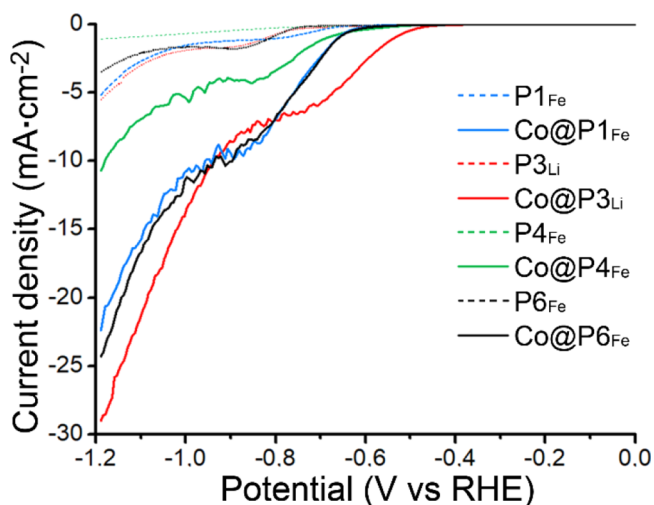


**Figure 6.** LSV curves of selected  $\text{Co@PX}$  vs  $\text{PX}$  materials ( $x = 1, 3, 4,$  and  $6$ ).

$-0.74$  V for  $\text{P4}_{\text{Fe}}$ ,  $-0.76$  V for  $\text{P6}_{\text{Fe}}$ , and  $-0.62$  V for  $\text{P3}_{\text{Li}}$ ). This suggested the catalytic HER activity of the  $\text{Co@P1,3,4,6}$  derivatives, induced by the presence of cobalt in the inner cavities of the corresponding porous materials and most likely associated to  $\text{Co(II)}$  reduction. The overpotentials to reach a current density of  $1 \text{ mA}\cdot\text{cm}^{-2}$  were  $0.68$  V for  $\text{Co@P4}_{\text{Fe}}$ ,  $0.66$  V for  $\text{Co@P1}_{\text{Fe}}$  and  $\text{Co@P6}_{\text{Fe}}$ , and  $0.53$  V for  $\text{Co@P3}_{\text{Li}}$ , relatively high compared to (i) other HER electrocatalysts working at neutral pH<sup>50,61</sup> (ii) related MOF<sup>62,63</sup> and COF<sup>43,61,64</sup> materials (working under kinetically more favorable strongly acidic or basic conditions), and (iii) the only reported noncarbonized POP-based material for electrochemical HER (containing intrinsically highly active Pt nanoparticles).<sup>46</sup> The high HER overpotentials of these cobalt-based materials could be tentatively explained either with the low density of catalytic sites, the low wettability, or the low electrical conductivity of the polymer materials.

In order to evaluate the durability of the catalysts and to confirm the effect of  $\text{P1,3,4,6}$  metallation on the HER performances on a longer timescale, controlled potential electrolysis (CPE) experiments were carried out on the  $\text{Co@P1,3,4,6}$  vs the respective  $\text{P1,3,4,6}$  materials at  $-0.68$  V vs

RHE during 8 h. Significant differences in current densities between the Co-containing and the metal-free versions of the material were observed only for the  $\text{P1}_{\text{Fe}}$  and  $\text{P3}_{\text{Li}}$  materials (Figure S40), which were thus the only ones behaving as stable HER catalysts. The amounts of produced  $\text{H}_2$  were measured by gas chromatography (Figure S41), which allowed to determine the HER Faradaic efficiency to be 82% for  $\text{Co@P1}_{\text{Fe}}$  ( $4.76 \times 10^{-5}$  mol  $\text{H}_2$  per 11.25 C) and 95% for  $\text{Co@P3}_{\text{Li}}$  ( $5.81 \times 10^{-5}$  mol  $\text{H}_2$  per 11.76 C). Turnover numbers (TONs) and frequencies (TOFs) could be estimated based on the hypothesis that each single cobalt center behaved as an active catalyst:  $\text{TON}_{\text{Co@P1}} = 1.1 \times 10^4$ ,  $\text{TOF}_{\text{Co@P1}} = 1.4 \times 10^3 \text{ h}^{-1}$ ,  $\text{TON}_{\text{Co@P3}} = 1.2 \times 10^4$ , and  $\text{TOF}_{\text{Co@P3}} = 1.5 \times 10^3 \text{ h}^{-1}$ . These catalytic parameters demonstrated a good intrinsic HER activity of each single active Co center<sup>50,53</sup> and a reasonable catalyst stability, even at noncompetitive overpotentials.

## CONCLUSIONS

In summary, we have prepared a series of porous materials with incorporated  $\text{P}=\text{O}$  functions aiming at binding metal centers with the purpose to generate hybrid materials suitable for application in the energy conversion domain. Different synthetic strategies were investigated to generate porous polymers. F-C polymerization with iron chloride, which is widely used in industrial applications, led to larger absorption capacity and a high surface area of up to  $990 \text{ m}^2/\text{g}$ . The detrimental issue of iron catalyst inactivation due to scavenging operated by the phosphines could be circumvented by the formation of the phosphine- $\text{BH}_3$  adduct, which was then used for the successful formation of polymer  $\text{P7}_{\text{Fe}}$ . The presented strategy opens the possibility to employ a wider array of phosphines for the generation of tailored phosphine oxide porous polymers. The presence of a homogeneous distribution of  $\text{P}=\text{O}$  moieties in the cavity allowed the functionalization of all of the polymers investigated with cobalt(II) ions using the impregnation method. In a proof-of-concept investigation,  $\text{Co@P1}_{\text{Fe}}$  and  $\text{Co@P3}_{\text{Li}}$  have shown an electrocatalytic HER activity under environmentally benign neutral pH conditions. To our knowledge, they represent a rare example of HER electrocatalysts based on noncarbonized POPs and including non-noble metals as active species. Although the catalytic performances of these materials are currently limited (high overpotentials), in perspective, their properties (porosity, surface area, density of binding sites, wettability, and electrical conductivity) can be tuned, both by exploring new monomer combinations and by the incorporation of other non-noble transition metals (like iron, molybdenum, and nickel, see Figure S33). These future investigations will have the objective of increasing (i) the density of catalytically active centers, (ii) their accessibility to substrates, and (iii) the activity of each single active center. The goal is also to extend the use of POPs to other electrodriven activation reactions (like ORR,  $\text{CO}_2\text{RR}$ ,  $\text{NRR}$ , etc.) toward efficient and sustainable small molecule conversion.

## EXPERIMENTAL SECTION

**General Methods.** Anhydrous solvents were dried and stored over molecular sieves ( $3 \text{ \AA}$ ), and all other reagents and solvents were used as received. Anhydrous iron(III) chloride was purchased from Sigma Aldrich and stored in a glovebox under nitrogen. Reactions performed under an inert atmosphere were carried out using Schlenk glassware using nitrogen

as the inert gas. Flash column chromatography was performed using silica gel (230–400 mesh). NMR experiments were performed on either a Bruker Avance 400 MHz instrument and JEOL 600 MHz ECZ600R instrument at 298 K. Chemical shifts are quoted in ppm relative to tetramethylsilane, using the solvent residual peak of  $\text{CDCl}_3$  ( $\delta_{\text{H}}$  7.26,  $\delta_{\text{C}}$  77.00) as a reference standard. TGA was performed with a PerkinElmer TGA 8000 and by heating the polymer (0.5–3 mg) from 30 to 600/800 °C in atmospheric pressure, with a T-ramp of 5 °C  $\text{min}^{-1}$  under oxygen flux (30 mL  $\text{min}^{-1}$ ). IR spectra were obtained with a Perkin Elmer spectrum two FT-IR spectrometer (diamond crystal) in the 4000–400  $\text{cm}^{-1}$  interval at room temperature.

**General Procedures for the Polymerization.** The products  $\text{P1}_{\text{Fe}}$ ,<sup>29</sup>  $\text{P2}_{\text{Al}}$ ,<sup>31</sup> and  $\text{P3}_{\text{Li}}$ <sup>30</sup> were prepared according to published procedures.  $\text{P4}_{\text{Fe}}$ ,  $\text{P7}_{\text{Fe}}$  and  $\text{P6}_{\text{Fe}}$  were prepared by reacting the organophosphine monomer, FDA, benzene, anhydrous  $\text{FeCl}_3$ , and anhydrous 1,2-dichloroethane as the solvent under the inert gas atmosphere ( $\text{N}_2$ ). The mixture was stirred at 80 °C for the required time.  $\text{P5}_{\text{Al}}$  was prepared by reacting the phosphine monomer, 1,4-bis(bromomethyl)-benzene, anhydrous  $\text{AlCl}_3$ , and anhydrous 1,2-dichloroethane as solvents under the inert gas atmosphere ( $\text{N}_2$ ). The mixture was stirred at 80 °C for the required time. The details of the synthesis and purification steps are reported in the Supporting Information (Figures S1–S9).

**Solid-State NMR.** Solid-state NMR experiments observing  $^{13}\text{C}$ ,  $^1\text{H}$ ,  $^{31}\text{P}$ , and  $^{19}\text{F}$  nuclei were performed using a Bruker Avance 300 instrument equipped with high-power amplifiers (1 kW) and a 4 mm double-resonance MAS probe.  $^{13}\text{C}\{^1\text{H}\}$  ramped-amplitude cross-polarization (CP) experiments were carried out at a spinning speed of 12.5 kHz using a 5 s recycle delay and 0.05–2 ms contact times. The  $^1\text{H}$  90° pulse length was 2.5  $\mu\text{s}$ . As an external chemical shift reference, crystalline polyethylene was set at 32.8 ppm. For a quantitative analysis, single-pulse excitation (SPE) MAS NMR spectra were performed using a recycle delay of 60 s.  $^{31}\text{P}\{^1\text{H}\}$  ramped-amplitude CP experiments were performed at a spinning speed of 12.5 kHz using a recycle delay of 5 s and a contact time of 8.5 ms.  $^1\text{H}$  MAS NMR spectra were performed at a spinning speed of 12.5 kHz using a recycle delay of 20 s. The  $^1\text{H}$  chemical shift was referenced to adamantane. The  $^{19}\text{F}$  MAS NMR spectrum of  $\text{P6}_{\text{Fe}}$  was performed at a spinning speed of 12.5 kHz using a recycle delay of 20 s. The 90° pulse for  $^{19}\text{F}$  was 2.5  $\mu\text{s}$ . The  $^{19}\text{F}$  chemical shift was referenced to sodium fluoride. Phase-modulated Lee–Goldburg (PMLG) heteronuclear  $^1\text{H}$ – $^{13}\text{C}$  correlation (HETCOR) experiments coupled with fast magic-angle spinning (MAS) allowed the recording of the 2D spectra with a high resolution in both  $^1\text{H}$  and  $^{13}\text{C}$  dimensions. The line widths of hydrogen resonances are on the order of 1–2 ppm, as obtained by homonuclear decoupling during  $t_1$ . The 2D  $^1\text{H}$ – $^{13}\text{C}$  PMLG HETCOR spectra were run with an LG period of 18.9  $\mu\text{s}$ . The efficient transfer of magnetization to the carbon nuclei was performed by applying the RAMP-CP sequence. Quadrature detection in  $t_1$  was achieved by the time proportional phase increment method (TPPI). The carbon signals were acquired during  $t_2$  under  $^1\text{H}$  decoupling by applying the two-pulse phase modulation scheme (TPPM). The 2D  $^1\text{H}$ – $^{13}\text{C}$  PMLG HETCOR NMR spectra of  $\text{P4}_{\text{Fe}}$  were conducted at 298 K under MAS conditions at 12.5 kHz with a contact time of 2 ms.

**Gas-Adsorption Measurements.**  $\text{N}_2$  adsorption isotherms at 77 K were collected on a sorption analyzer

(Micromeritics ASAP 2020). The samples were treated overnight at 100 °C under high vacuum before adsorption experiments ( $p < 5 \mu\text{bar}$ ). Surface areas were calculated from the  $\text{N}_2$  adsorption isotherm at 77 K using the data in the pressure range  $P/P_0$  from 0.015 to 0.1, according to the BET and Langmuir models. The total pore volume was calculated from the  $\text{N}_2$  adsorption isotherms at 77 K using the nonlocal density functional theory (NLDFIT) method with the carbon slit pore model up to  $P/P_0$  0.98.

**Functionalization with Co(II).** To 40–50 mg of porous polymers  $\text{P1}$ – $\text{P6}$ , a 0.35 M  $\text{CoCl}_2 \cdot 6 \text{H}_2\text{O}$  solution (3 mL; 1.05 mmol), and 3 mL of dry THF were added under an inert atmosphere, forming a blue reaction mixture. The system was stirred at r.t. for 48 h and then was washed with THF and centrifuged until the supernatant became colorless. After this time, the solvent was discarded, and the solid was dried under vacuum for 4 days. The functionalization of  $\text{P3}_{\text{Li}}$  with other transition metals [Ni(II), Mo(III), and Fe(II)] is reported in the Supporting Information (Figure S33).

**Characterization of the Metal Content.** Scanning electron microscopy (SEM) experiments were performed using an ESEM instrument Quanta 250 FEG (FEI, Hillsboro, OR) equipped with an energy-dispersive spectrometer for X-ray microanalysis (Bruker Nano GmbH, Berlin, Germany). The energy-dispersive X-ray spectrometer is equipped with a QUANTAX XFlash 6 | 30 detector with energy resolution  $\leq 126$  eV full width at half maximum (FWHM) at  $\text{Mn}\alpha$ . The spectra were collected and analyzed using ESPRIT 1.9 software (Bruker Nano GmbH). ICP-AES analyses were performed with an ULTIMA 2 instrument JOBIN YVON in the radial configuration, with a JY 2501 monochromator calibrated against carbon lines. The optical path was continuously purged with nitrogen (2 L/min). The samples of the functionalized frameworks were dissolved in 2 mL of a mixture of  $\text{HNO}_3$  65% and  $\text{H}_2\text{O}_2$  30% and then heated by microwave irradiation (Milestone, MLS-1200 MEGA, equipped with TFM inner vessels). Calibration was performed with standard solutions, 10% of  $\text{HNO}_3$  on six different metal concentration levels, ranging from 0.5 to 100 mg/L. No significant spectral interferences were detected. Data were acquired by considering the following emission lines: Fe 238.204 nm, Co 228.616 nm, and Mo 202.030 nm. Data acquisition and processing were performed using the ICP JY v 5.4.2 software (Jobin Yvon).

**Electrochemical Measurements.** Electrochemical measurements were performed using an electrochemical workstation (Metrohm-Autolab potentiostat/galvanostat, PGSTAT100N) with a standard three-electrode setup, with Ag/AgCl (in 3.5 M KCl solution) as the reference electrode, a platinum plate as the counter electrode, and a glassy carbon electrode (GCE, 3 mm in diameter) coated with as-prepared catalysts as the working electrode. All the measurements were carried out in 0.1 M phosphate buffer (pH 6.93) and conducted in an argon-saturated solution at ambient temperature. In a typical experiment, 5 mg of the target material and 5 mg of carbon black powder (Vulcan XC 72R) were dispersed in 950  $\mu\text{L}$  of isopropanol and 50  $\mu\text{L}$  of Nafion solution (5 wt. %). The mixture was vigorously sonicated for about 1 h to form a “homogeneous” ink suspension. The obtained ink (5  $\mu\text{L}$ ) was drop-casted onto a GCE (3 mm diameter, mass loading of  $\sim 90 \mu\text{g cm}^{-2}$ ), previously polished with diamond paste, sonicated in water for 10 min, washed with acetone, and oven-dried. All the measurements were referred to the

reversible hydrogen electrode (RHE) using the following equation:

$$E(\text{RHE}) = E(\text{Ag/AgCl}) + E_0(\text{Ag/AgCl}) + 0.059 \text{ V} \\ \times \text{pH}$$

Each newly prepared electrode was first stabilized by cyclic voltammetry (CV) between 0 and  $-1.18 \text{ V}$  vs RHE at a scan rate of  $50 \text{ mV s}^{-1}$  until the CV curves remain roughly stable (10 cycles). After this step, LSV experiments were carried out at a scan rate of  $5 \text{ mV s}^{-1}$  in the same potential window. The linear portions of the Tafel plots (i.e., overpotential vs  $\log(|j|)$  plot), as derived from iR-corrected LSV curves, were analyzed using the fitting Tafel equation:

$$\eta = b \times \log(|j|) + A$$

where  $j$  is the current density ( $\text{mA cm}^{-2}$ ),  $\eta$  is the overpotential vs RHE,  $b$  is the Tafel slope, and  $A$  is the intercept of the linear regression. For  $\text{H}_2$  quantification, a custom-made four-neck cell was used and equipped with rubber septa, allowing for the introduction of three electrodes as well as the gas inlet and outlet tubing. The counter electrode (Pt) was separated from the working electrode compartment with a glass frit.

The free volume of the closed cell after fitting the septa and electrodes was determined (38.0 mL), and the electrolyte (15.0 mL, 0.1 M phosphate buffer) was introduced. The electrolyte was purged with  $\text{N}_2$  ( $10 \text{ mL min}^{-1}$ ) for 30 min before conditioning the working electrode (3 mm GC, coated with the desired material) as mentioned above. The electrolyte was further purged with  $\text{N}_2$  for 5 min before running 8 h long CPE at  $-0.68 \text{ V}$  vs RHE. The quantification of produced  $\text{H}_2$  was performed using a Perkin Elmer Clarus 580 gas chromatograph. CPE was run under constant  $\text{N}_2$  purging ( $5 \text{ mL min}^{-1}$ ), and automated injections were programmed to sample the composition of the exhausting gas mixture every 2 min. The instant production of  $\text{H}_2$  could therefore be monitored over time, and the total quantity of  $\text{H}_2$  produced during the CPE was determined upon integration over 8 h of the experiments.

## ■ ASSOCIATED CONTENT

### SI Supporting Information

The Supporting Information is available free of charge at <https://pubs.acs.org/doi/10.1021/acsomega.1c06522>.

Synthesis of polymers, solid-state NMR, FT-IR spectra, TGA profiles, EDS spectra, ICP analysis of the loaded polymers, and controlled potential electrolysis (PDF)

### Accession Codes

CCDC 2100398 contain the supplementary crystallographic data for this study. These data can be obtained free of charge via [www.ccdc.ca-mac.ac.uk/data\\_request/cif](http://www.ccdc.ca-mac.ac.uk/data_request/cif) by emailing [data\\_request@ccdc.cam.ac.uk](mailto:data_request@ccdc.cam.ac.uk) or by contacting The Cambridge Crystallographic Data Centre, 12, Union Road, Cambridge CB2 1EZ, UK; fax: +441223 336033.

## ■ AUTHOR INFORMATION

### Corresponding Author

Luciano Marchiò – Department of Chemistry, Life Sciences and Environmental Sustainability, University of Parma, Parma 43124, Italy; [orcid.org/0000-0002-0025-1104](https://orcid.org/0000-0002-0025-1104); Email: [luciano.marchio@unipr.it](mailto:luciano.marchio@unipr.it)

## Authors

Giulia Bonfant – Department of Chemistry, Life Sciences and Environmental Sustainability, University of Parma, Parma 43124, Italy; [orcid.org/0000-0001-5108-8354](https://orcid.org/0000-0001-5108-8354)

Davide Balestri – Department of Chemistry, Life Sciences and Environmental Sustainability, University of Parma, Parma 43124, Italy

Jacopo Perego – Department of Materials Science, University of Milan Bicocca, Milan 20215, Italy

Angiolina Comotti – Department of Materials Science, University of Milan Bicocca, Milan 20215, Italy; [orcid.org/0000-0002-8396-8951](https://orcid.org/0000-0002-8396-8951)

Silvia Bracco – Department of Materials Science, University of Milan Bicocca, Milan 20215, Italy; [orcid.org/0000-0002-2575-6424](https://orcid.org/0000-0002-2575-6424)

Matthieu Koepf – Laboratoire de Chimie et Biologie des Métaux, University of Grenoble Alpes, CNRS, CEA, IRIG, Grenoble 38000, France

Marcello Gennari – Département de Chimie Moléculaire, University of Grenoble Alpes, UMR CNRS 5250, Grenoble 38000, France; [orcid.org/0000-0001-5205-1123](https://orcid.org/0000-0001-5205-1123)

Complete contact information is available at:

<https://pubs.acs.org/10.1021/acsomega.1c06522>

## Notes

The authors declare no competing financial interest.

## ■ ACKNOWLEDGMENTS

This work was benefited from the equipment and framework of the COMP-HUB Initiative (UNIPR) and from the project “Materials for Energy” (UNIMIB) funded by the “Departments of Excellence” (MIUR, 2018-2022) and “Enhancing Photosynthesis” (Lombardy Region, 2021-2023). Chiesi Farmaceutici SpA is acknowledged for the support of the D8 Venture X-ray equipment. Financial support for this work was provided by the Agence Nationale de la Recherche (ANR-15-IDEX-02; Labex ARCANE). M.K. is grateful to Jennifer Fize for her guidance in setting up the bulk electrolysis experiments and help with the GC analysis.

## ■ REFERENCES

- (1) Xu, R.; Pang, W.; Yu, J.; Huo, Q.; Chen, J. *Chemistry of Zeolites and Related Porous Materials*; John Wiley & Sons, Ltd: Chichester, UK, 2007.
- (2) Wang, Q.; Astruc, D. State of the Art and Prospects in Metal-Organic Framework (MOF)-Based and MOF-Derived Nanocatalysis. *Chem. Rev.* **2020**, *120*, 1438–1511.
- (3) Furukawa, H.; Cordova, K. E.; O’Keeffe, M.; Yaghi, O. M. The Chemistry and Applications of Metal-Organic Frameworks. *Science* **2013**, *341*, No. 1230444.
- (4) Kang, Y. S.; Lu, Y.; Chen, K.; Zhao, Y.; Wang, P.; Sun, W. Y. Metal–Organic Frameworks with Catalytic Centers: From Synthesis to Catalytic Application. *Coord. Chem. Rev.* **2019**, *378*, 262–280.
- (5) Chen, X.; Jiang, H.; Hou, B.; Gong, W.; Liu, Y.; Cui, Y. Boosting Chemical Stability, Catalytic Activity, and Enantioselectivity of Metal–Organic Frameworks for Batch and Flow Reactions. *J. Am. Chem. Soc.* **2017**, *139*, 13476–13482.
- (6) Das, S.; Heasman, P.; Ben, T.; Qiu, S. Porous Organic Materials: Strategic Design and Structure–Function Correlation. *Chem. Rev.* **2017**, *117*, 1515–1563.
- (7) Geng, K.; He, T.; Liu, R.; Dalapati, S.; Tan, K. T.; Li, Z.; Tao, S.; Gong, Y.; Jiang, Q.; Jiang, D. Covalent Organic Frameworks: Design, Synthesis, and Functions. *Chem. Rev.* **2020**, *120*, 8814–8933.



- (8) Diercks, C. S.; Yaghi, O. M. The Atom, the Molecule, and the Covalent Organic Framework. *Science* **2017**, *355*, No. eaal1585.
- (9) Zhou, H. C. J.; Kitagawa, S. Metal-Organic Frameworks (MOFs). *Chem. Soc. Rev.* **2014**, *43*, 5415–5418.
- (10) Kitagawa, S.; Kitaura, R.; Noro, S. Functional Porous Coordination Polymers. *Angew. Chem., Int. Ed.* **2004**, *43*, 2334–2375.
- (11) Cui, Y.; Li, B.; He, H.; Zhou, W.; Chen, B.; Qian, G. Metal-Organic Frameworks as Platforms for Functional Materials. *Acc. Chem. Res.* **2016**, *49*, 483–493.
- (12) Li, B.; Gong, R.; Wang, W.; Huang, X.; Zhang, W.; Li, H.; Hu, C.; Tan, B. A New Strategy to Microporous Polymers: Knitting Rigid Aromatic Building Blocks by External Cross-Linker. *Macromolecules* **2011**, *44*, 2410–2414.
- (13) Tian, Y.; Zhu, G. Porous Aromatic Frameworks (PAFs). *Chem. Rev.* **2020**, *120*, 8934–8986.
- (14) Ben, T.; Qiu, S. Porous Aromatic Frameworks: Synthesis, Structure and Functions. *CrystEngComm* **2013**, *15*, 17–26.
- (15) Ben, T.; Ren, H.; Ma, S.; Cao, D.; Lan, J.; Jing, X.; Wang, W.; Xu, J.; Deng, F.; Simmons, J. M.; Qiu, S.; Zhu, G. Targeted Synthesis of a Porous Aromatic Framework with High Stability and Exceptionally High Surface Area. *Angew. Chem., Int. Ed.* **2009**, *48*, 9457–9460.
- (16) Comotti, A.; Castiglioni, F.; Bracco, S.; Perego, J.; Pedrini, A.; Negroni, M.; Sozzani, P. Fluorinated Porous Organic Frameworks for Improved CO<sub>2</sub> and CH<sub>4</sub> Capture. *Chem. Commun.* **2019**, *55*, 8999–9002.
- (17) Comotti, A.; Bracco, S.; Ben, T.; Qiu, S.; Sozzani, P. Molecular Rotors in Porous Organic Frameworks. *Angew. Chem., Int. Ed.* **2014**, *53*, 1043–1047.
- (18) Zhang, Y.; Riduan, S. N. Functional Porous Organic Polymers for Heterogeneous Catalysis. *Chem. Soc. Rev.* **2012**, *41*, 2083–2094.
- (19) Giri, A.; Sahoo, A.; Dutta, T. K.; Patra, A. Cavitand and Molecular Cage-Based Porous Organic Polymers. *ACS Omega* **2020**, *5*, 28413–28424.
- (20) Zhu, T.; Shi, B.; Wu, H.; You, X.; Wang, X.; Fan, C.; Peng, Q.; Jiang, Z. Highly Proton Conductive Phosphoric Acid Porous Organic Polymers via Knitting Method. *Ind. Eng. Chem. Res.* **2021**, *60*, 6337–6343.
- (21) Pan, X.; Ding, C.; Zhang, Z.; Ke, H.; Cheng, G. Functional Porous Organic Polymer with High S and N for Reversible Iodine Capture. *Microporous Mesoporous Mater.* **2020**, *300*, No. 110161.
- (22) Wang, T.-X.; Liang, H.-P.; Anito, D. A.; Ding, X.; Han, B.-H. Emerging Applications of Porous Organic Polymers in Visible-Light Photocatalysis. *J. Mater. Chem. A* **2020**, *8*, 7003–7034.
- (23) Kaur, P.; Hupp, J. T.; Nguyen, S. T. Porous Organic Polymers in Catalysis: Opportunities and Challenges. *ACS Catal.* **2011**, *1*, 819–835.
- (24) Atilgan, A.; Cetin, M. M.; Yu, J.; Beldjoudi, Y.; Liu, J.; Stern, C. L.; Cetin, F. M.; Islamoglu, T.; Farha, O. K.; Deria, P.; et al. Post-Synthetically Elaborated BODIPY-Based Porous Organic Polymers (POPs) for the Photochemical Detoxification of a Sulfur Mustard Simulant. *J. Am. Chem. Soc.* **2020**, *142*, 18554.
- (25) Sarkar, C.; Shit, S. C.; Das, N.; Mondal, J. Presenting Porous-Organic-Polymers as next-Generation Invigorating Materials for Nanoreactors. *Chem. Commun.* **2021**, *57*, 8550.
- (26) Jing, L. P.; Sun, J. S.; Sun, F.; Chen, P.; Zhu, G. Porous Aromatic Framework with Mesopores as a Platform for a Super-Efficient Heterogeneous Pd-Based Organometallic Catalysis. *Chem. Sci.* **2018**, *9*, 3523–3530.
- (27) Karakhanov, E.; Kardasheva, Y.; Kulikov, L.; Maximov, A.; Zolotukhina, A.; Vinnikova, M.; Ivanov, A. Sulfide Catalysts Supported on Porous Aromatic Frameworks for Naphthalene Hydroprocessing. *Catalysts* **2016**, *6*, 122.
- (28) Kramer, S.; Bennedsen, N. R.; Kegnæs, S. Porous Organic Polymers Containing Active Metal Centers as Catalysts for Synthetic Organic Chemistry. *ACS Catal.* **2018**, *8*, 6961–6982.
- (29) Li, B.; Guan, Z.; Wang, W.; Yang, X.; Hu, J.; Tan, B.; Li, T. Highly Dispersed Pd Catalyst Locked in Knitting Aryl Network Polymers for Suzuki-Miyaura Coupling Reactions of Aryl Chlorides in Aqueous Media. *Adv. Mater.* **2012**, *24*, 3390–3395.
- (30) Fritsch, J.; Drache, F.; Nickerl, G.; Böhlmann, W.; Kaskel, S. Porous Phosphorus-Based Element Organic Frameworks: A New Platform for Transition Metal Catalysts Immobilization. *Microporous Mesoporous Mater.* **2013**, *172*, 167–173.
- (31) Yang, Y.; Wang, T.; Jing, X.; Zhu, G. Phosphine-Based Porous Aromatic Frameworks for Gold Nanoparticle Immobilization with Superior Catalytic Activities. *J. Mater. Chem. A* **2019**, *7*, 10004–10009.
- (32) Kumar, P.; Das, A.; Maji, B. Phosphorus Containing Porous Organic Polymers: Synthetic Techniques and Applications in Organic Synthesis and Catalysis. *Org. Biomol. Chem.* **2021**, *19*, 4174–4192.
- (33) Katagiri, K.; Matsuo, N.; Kawahata, M.; Masu, H.; Yamaguchi, K. Aqua Coordination to Attenuate the Luminescence Properties of Europium (iii)-Phosphine Oxide Porous Coordination Polymers. *New J. Chem.* **2017**, *41*, 8305–8311.
- (34) Zhang, Q.; Yang, Y.; Zhang, S. Novel Functionalized Microporous Organic Networks Based on Triphenylphosphine. *Chem. – Eur. J.* **2013**, *19*, 10024–10029.
- (35) Zhang, W.; Mu, Y.; He, X.; Chen, P.; Zhao, S.; Huang, C.; Wang, Y.; Chen, J. Robust Porous Polymers Bearing Phosphine Oxide/Chalcogenide Ligands for Volatile Iodine Capture. *Chem. Eng. J.* **2020**, *379*, No. 122365.
- (36) Chen, H.; Liang, X.; Liu, Y.; Ai, X.; Asefa, T.; Zou, X. Active Site Engineering in Porous Electrocatalysts. *Adv. Mater.* **2020**, *32*, No. 2002435.
- (37) Morozan, A.; Jaouen, F. Metal Organic Frameworks for Electrochemical Applications. *Energy Environ. Sci.* **2012**, *5*, 9269–9290.
- (38) Downes, C. A.; Marinescu, S. C. Electrocatalytic Metal-Organic Frameworks for Energy Applications. *ChemSusChem* **2017**, *10*, 4374–4392.
- (39) Liao, P.-Q.; Shen, J.-Q.; Zhang, J.-P. Metal-Organic Frameworks for Electrocatalysis. *Coord. Chem. Rev.* **2018**, *373*, 22–48.
- (40) Sun, F.; Li, Q.; Xue, H.; Pang, H. Pristine Transition-Metal-Based Metal-Organic Frameworks for Electrocatalysis. *ChemElectroChem* **2019**, *6*, 1273–1299.
- (41) Wei, Y. S.; Zhang, M.; Zou, R.; Xu, Q. Metal-Organic Framework-Based Catalysts with Single Metal Sites. *Chem. Rev.* **2020**, *120*, 12089–12174.
- (42) Lin, C.-Y.; Zhang, D.; Zhao, Z.; Xia, Z. Covalent Organic Framework Electrocatalysts for Clean Energy Conversion. *Adv. Mater.* **2018**, *30*, No. 1703646.
- (43) Cui, X.; Lei, S.; Wang, A. C.; Gao, L.; Zhang, Q.; Yang, Y.; Lin, Z. Emerging Covalent Organic Frameworks Tailored Materials for Electrocatalysis. *Nano Energy* **2020**, *70*, No. 104525.
- (44) Wang, D.-G.; Qiu, T.; Guo, W.; Liang, Z.; Tabassum, H.; Xia, D.; Zou, R. Covalent Organic Framework-Based Materials for Energy Applications. *Energy Environ. Sci.* **2021**, *14*, 688–728.
- (45) Soliman, A. B.; Haikal, R. R.; Hassan, Y. S.; Alkordi, M. H. The Potential of a Graphene-Supported Porous-Organic Polymer (POP) for CO<sub>2</sub> Electrocatalytic Reduction. *Chem. Commun.* **2016**, *52*, 12032–12035.
- (46) Fang, H.; Chen, J.; Balogun, M.-S.; Tong, Y.-X.; Zhang, J. Covalently Modified Electrode with Pt Nanoparticles Encapsulated in Porous Organic Polymer for Efficient Electrocatalysis. *ACS Appl. Nano Mater.* **2018**, *1*, 6477–6482.
- (47) Singh, A.; Samanta, D.; Maji, T. K. Realization of Oxygen Reduction and Evolution Electrocatalysis by In Situ Stabilization of Co Nanoparticles in a Redox-Active Donor-Acceptor Porous Organic Polymer. *ChemElectroChem* **2019**, *6*, 3756–3763.
- (48) Guo, J.; Huo, F.; Cheng, Y.; Xiang, Z. PAF-1 as Oxygen Tank to in-Situ Synthesize Edge-Exposed O-MoS<sub>2</sub> for Highly Efficient Hydrogen Evolution. *Catal. Today* **2020**, *347*, 56–62.
- (49) Horibe, T.; Nakagawa, K.; Hazeyama, T.; Takeda, K.; Ishihara, K. An Enantioselective Oxidative Coupling Reaction of 2-Naphthol Derivatives Catalyzed by Chiral Diphosphine Oxide-Iron (ii) Complexes. *Chem. Commun.* **2019**, *55*, 13677–13680.
- (50) Callejas, J. F.; McEnaney, J. M.; Read, C. G.; Crompton, J. C.; Biacchi, A. J.; Popczun, E. J.; Gordon, T. R.; Lewis, N. S.; Schaak, R.

E. Electrocatalytic and Photocatalytic Hydrogen Production from Acidic and Neutral-pH Aqueous Solutions Using Iron Phosphide Nanoparticles. *ACS Nano* **2014**, *8*, 11101–11107.

(51) Fan, M.; Gao, R.; Zou, Y.-C.; Wang, D.; Bai, N.; Li, G.-D.; Zou, X. An Efficient Nanostructured Copper (I) Sulfide-Based Hydrogen Evolution Electrocatalyst at Neutral pH. *Electrochim. Acta* **2016**, *215*, 366–373.

(52) Liu, J.; Zhu, D.; Ling, T.; Vasileff, A.; Qiao, S.-Z. S-NiFe<sub>2</sub>O<sub>4</sub> Ultra-Small Nanoparticle Built Nanosheets for Efficient Water Splitting in Alkaline and Neutral pH. *Nano Energy* **2017**, *40*, 264–273.

(53) Zhang, R.; Wang, X.; Yu, S.; Wen, T.; Zhu, X.; Yang, F.; Sun, X.; Wang, X.; Hu, W. Ternary NiCo<sub>2</sub> P<sub>x</sub> Nanowires as pH-Universal Electrocatalysts for Highly Efficient Hydrogen Evolution Reaction. *Adv. Mater.* **2017**, *29*, No. 1605502.

(54) Zhou, Z.; Pei, Z.; Wei, L.; Zhao, S.; Jian, X.; Chen, Y. Electrocatalytic Hydrogen Evolution under Neutral pH Conditions: Current Understandings, Recent Advances, and Future Prospects. *Energy Environ. Sci.* **2020**, *13*, 3185–3206.

(55) Bracco, S.; Piga, D.; Bassanetti, I.; Perego, J.; Comotti, A.; Sozzani, P. Porous 3D Polymers for High Pressure Methane Storage and Carbon Dioxide Capture. *J. Mater. Chem. A* **2017**, *5*, 10328–10337.

(56) Perego, J.; Piga, D.; Bracco, S.; Sozzani, P.; Comotti, A. Expandable Porous Organic Frameworks with Built-in Amino and Hydroxyl Functions for CO<sub>2</sub> and CH<sub>4</sub> Capture. *Chem. Commun.* **2018**, *54*, 9321–9324.

(57) Perego, J.; Bracco, S.; Comotti, A.; Piga, D.; Bassanetti, I.; Sozzani, P. Anionic Polymerization in Porous Organic Frameworks: A Strategy to Fabricate Anchored Polymers and Copolymers. *Angew. Chem.* **2021**, *133*, 6182–6188.

(58) Vicente, J. A.; Mlonka, A.; Gunaratne, H. Q. N.; Swadźba-Kwaśny, M.; Nockemann, P. Phosphine Oxide Functionalised Imidazolium Ionic Liquids as Tunable Ligands for Lanthanide Complexation. *Chem. Commun.* **2012**, *48*, 6115.

(59) Bowden, A.; Horton, P. N.; Platt, A. W. G. Lanthanide Nitrate Complexes of Tri-Isobutylphosphine Oxide: Solid State and CD<sub>2</sub>Cl<sub>2</sub> Solution Structures. *Inorg. Chem.* **2011**, *50*, 2553–2561.

(60) Platt, A. W. G. Lanthanide Phosphine Oxide Complexes. *Coord. Chem. Rev.* **2017**, *340*, 62–78.

(61) Bhunia, S.; Das, S. K.; Jana, R.; Peter, S. C.; Bhattacharya, S.; Addicoat, M.; Bhaumik, A.; Pradhan, A. Electrochemical Stimuli-Driven Facile Metal-Free Hydrogen Evolution from Pyrene-Porphyrin-Based Crystalline Covalent Organic Framework. *ACS Appl. Mater. Interfaces* **2017**, *9*, 23843–23851.

(62) Nivetha, R.; Gothandapani, K.; Raghavan, V.; Jacob, G.; Sellappan, R.; Bhardwaj, P.; Pitchaimuthu, S.; Kannan, A. N. M.; Jeong, S. K.; Grace, A. N. Highly Porous MIL-100 (Fe) for the Hydrogen Evolution Reaction (HER) in Acidic and Basic Media. *ACS Omega* **2020**, *5*, 18941–18949.

(63) Chen, K.; Ray, D.; Ziebel, M. E.; Gaggioli, C. A.; Gagliardi, L.; Marinescu, S. C. Cu [Ni (2, 3-Pyrazinedithiolate)<sub>2</sub>] Metal–Organic Framework for Electrocatalytic Hydrogen Evolution. *ACS Appl. Mater. Interfaces* **2021**, *13*, 34419–34427.

(64) Wang, A.; Cheng, L.; Zhao, W.; Shen, X.; Zhu, W. Electrochemical Hydrogen and Oxygen Evolution Reactions from a Cobalt-Porphyrin-Based Covalent Organic Polymer. *J. Colloid Interface Sci.* **2020**, *579*, 598–606.